



**HAL**  
open science

## Parallel on-chip micropipettes enabling quantitative multiplexed characterization of vesicle mechanics and cell aggregates rheology

Sylvain Landiech, Marianne Elias, Pierre Lapèze, Hajar Ajiyel, Marine Plancke, Blanca González-Bermúdez, Adrian Laborde, Fabien Mesnilgrete, David Bourrier, Debora Berti, et al.

### ► To cite this version:

Sylvain Landiech, Marianne Elias, Pierre Lapèze, Hajar Ajiyel, Marine Plancke, et al.. Parallel on-chip micropipettes enabling quantitative multiplexed characterization of vesicle mechanics and cell aggregates rheology. *APL Bioengineering*, 2024, 8 (2), pp.026122. 10.1063/5.0193333 . hal-04616249

**HAL Id: hal-04616249**

**<https://hal.science/hal-04616249v1>**

Submitted on 18 Jun 2024

**HAL** is a multi-disciplinary open access archive for the deposit and dissemination of scientific research documents, whether they are published or not. The documents may come from teaching and research institutions in France or abroad, or from public or private research centers.

L'archive ouverte pluridisciplinaire **HAL**, est destinée au dépôt et à la diffusion de documents scientifiques de niveau recherche, publiés ou non, émanant des établissements d'enseignement et de recherche français ou étrangers, des laboratoires publics ou privés.



Distributed under a Creative Commons Attribution - NonCommercial 4.0 International License

This is the author's peer reviewed, accepted manuscript. However, the online version of record will be different from this version once it has been copyedited and typeset.

PLEASE CITE THIS ARTICLE AS DOI: 10.1063/1.5019333

1 **Parallel on-chip micropipettes enabling quantitative multiplexed**  
 2 **characterization of vesicle mechanics and cell aggregates rheology**

3 Sylvain Landiech<sup>1†</sup>, Marianne Elias<sup>1†</sup>, Pierre Lapèze<sup>1</sup>, Hajar Ajiye<sup>1</sup>, Marine Plancke<sup>1</sup>, Blanca  
 4 González-Bermúdez<sup>2</sup>, Adrian Laborde<sup>1</sup>, Fabien Mesnilgrente<sup>1</sup>, David Bourrier<sup>1</sup>, Debora Berti<sup>3</sup>,  
 5 Costanza Montis<sup>3</sup>, Laurent Mazon<sup>1</sup>, Jérémy Baldo<sup>1</sup>, Clément Roux<sup>4</sup>, Morgan Delarue<sup>1</sup>, Pierre  
 6 Joseph<sup>1\*</sup>

7 <sup>†</sup>These two authors contributed equally.

8 \*Corresponding author [pierre.joseph@laas.fr](mailto:pierre.joseph@laas.fr)

9 **Affiliations**

10 <sup>1</sup> LAAS-CNRS, Université de Toulouse, CNRS, Toulouse, France

11 <sup>2</sup> Center for Biomedical Technology, Universidad Politécnica de Madrid, Pozuelo de Alarcón,  
 12 Spain and Department of Materials Science, ETSI de Caminos, Canales y Puertos, Universidad  
 13 Politécnica de Madrid, Madrid, Spain

14 <sup>3</sup> CSGI and Department of Chemistry, University of Florence, Sesto Fiorentino, Italy

15 <sup>4</sup> SoftMat, Université de Toulouse, CNRS, UPS, Toulouse, France

16

17 **Abstract**

18 Micropipette aspiration (MPA) is one of the gold standards for quantifying biological samples'  
 19 mechanical properties, which are crucial from the cell membrane scale to the multicellular  
 20 tissue. However, relying on the manipulation of individual home-made glass pipettes, MPA  
 21 suffers from low throughput and no automation. Here, we introduce the sliding insert  
 22 micropipette aspiration (SIMPA) method, which permits parallelization and automation, thanks  
 23 to the insertion of tubular pipettes, obtained by photolithography, within microfluidic channels.  
 24 We show its application both at the lipid bilayer level, by probing vesicles to measure  
 25 membrane bending and stretching moduli, and at the tissue level by quantifying the  
 26 viscoelasticity of 3D cell aggregates. This approach opens the way to high-throughput,  
 27 quantitative mechanical testing of many types of biological samples, from vesicles and  
 28 individual cells to cell aggregates and explants, under dynamic physico-chemical stimuli.

29

30 **Introduction**

31 Mechanics is ubiquitously at play in biology, from the level of cell membranes to the tissue  
 32 scale. At the cell scale, response to stimuli is related to its cytoskeleton and nucleus but also  
 33 strongly depends upon the deformability of its membrane<sup>1</sup>. At the multicellular scale, the  
 34 capacity of cell assemblies to deform and flow is a determining factor in tissue homeostasis and  
 35 evolution. This idea applies to developmental biology, since embryo morphogenesis is strongly  
 36 intertwined with spatiotemporal changes and heterogeneity in fluidity<sup>2,3</sup>. It is also an essential  
 37 ingredient for pathological situations such as solid cancers: the ability of cells to deform and  
 38 spread, or jam, is key in disease progression<sup>4</sup>. Tissue rheology can thus be envisioned as a  
 39 diagnostics tool<sup>5</sup>, or even to assist the prognosis of metastasis<sup>6</sup>.

40 Thus, strong efforts have been made in the last decades to engineer quantitative tools assessing  
 41 mechanical properties of cell membranes<sup>7</sup>, cells<sup>8</sup>, and cell aggregates<sup>9</sup>, often relying on

This is the author's peer reviewed, accepted manuscript. However, the online version of record will be different from this version once it has been copyedited and typeset.

PLEASE CITE THIS ARTICLE AS DOI: 10.1063/1.5019333

42 analogies with soft matter as proposed in Steinberg's pioneering work<sup>10</sup>, and on concepts of  
43 rheology<sup>11</sup>. One popular technique is micropipette aspiration MPA<sup>12-14</sup>, both at cell and tissue  
44 scale. MPA measures to what extent a vesicle, a cell, or a tissue enters a glass tube upon  
45 aspiration. It permits quantifying: bending and stretching rigidity for lipid vesicles mimicking  
46 cell membranes; apparent Young's modulus and effective viscosity for single cells<sup>8</sup>; surface  
47 tension, elasticity and viscosity for 3D cell aggregates<sup>15</sup>. MPA is one of the gold standards  
48 because it is quantitative, and it probes locally a zone that can be chosen. It also enables to some  
49 extent the change of solution surrounding the sample, and it can be coupled to other techniques  
50 like optical tweezers. However, it requires a complex dedicated setup: microscope,  
51 micromanipulator, and precise control of the pressure in the aspiration tube<sup>15</sup>. The control of  
52 the physico-chemical environment in real time requires several micromanipulators, and the  
53 concentration of chemicals injected around the sample is non-homogeneous. Most importantly,  
54 MPA suffers from very low throughput (~20 tests/h for single cells<sup>8</sup>, a few tests/h for vesicles,  
55 and less than one test/h for cell aggregates<sup>15</sup>) since objects are intrinsically probed one by one,  
56 which can be limiting due to the high sample-to-sample variability that is often typical of  
57 biological systems.

58

59 Consequently, approaches to integrate micropipettes in microfluidic devices have been  
60 proposed in the very last years. They target the above-mentioned limitations by designing  
61 channels enabling parallel trapping and fluid control at the cell (or cell aggregate) scale. A  
62 design relying on 3-level fabrication was developed ten years ago by Lee *et al.* for cells<sup>16</sup>, which  
63 we improved in terms of alignment for the study of Giant Unilamellar Vesicles (GUV)<sup>17</sup>. Boot  
64 *et al.* have recently adapted it to 3D cell aggregates<sup>18</sup>. While for this design microfluidics  
65 permits automation of objects injection, the rectangular geometry has intrinsic limitations: a  
66 quantitative analysis is complicated and some flow remains at the corner of the traps  
67 constituting the pipette, even though recent work described the different regimes of clogging  
68 rectangles with soft objects<sup>19</sup>. A 2-level design was used to probe the viscoelasticity of cell  
69 nuclei in parallel thanks to constrictions<sup>20</sup>, simpler to implement than the previous one but still  
70 not fully quantitative. To relate the microscopic configuration to mechanical properties, 2D  
71 geometries permitting optical access combined with rheological measurements were used to  
72 characterize cell aggregate rearrangements<sup>21</sup> or vesicle prototissues<sup>22</sup>, but their extension to  
73 more realistic 3D tissues is far from obvious. Indeed, standard microfabrication techniques are  
74 planar, which limits the possibility of properly integrating circular traps. 3D printing  
75 technologies are associated with long writing time (several hours) for the resolution required  
76 here, and can hardly ensure nanometric surface roughness needed to properly aspirate vesicles  
77 or cell aggregates. As a way to eliminate the need for fluid confinement by surfaces, virtual  
78 walls microfluidics has recently been demonstrated to characterize both cell and spheroid  
79 mechanics<sup>23</sup>, with quite a high throughput but limited to a global probing of objects.

80

81 Thus, a micropipette aspiration method, quantitative but with a higher throughput than classical  
82 MPA, is still to be developed. We describe in this paper the SIMPA technology (sliding insert  
83 micropipette aspiration) addressing the above-mentioned requirements, both at the scales of  
84 vesicles and multicellular aggregates. It relies on the "sliding walls" proposed by Venzac *et*  
85 *al.*<sup>24</sup>, inserting sliding elements within PDMS chips. Here, rather than reconfigurability, which  
86 was the strong point raised in<sup>24</sup>, and which for instance permitted studying confined tissue  
87 growth<sup>25</sup>, we specifically exploited the particular microfabrication features of the approach.

This is the author's peer reviewed, accepted manuscript. However, the online version of record will be different from this version once it has been copyedited and typeset.

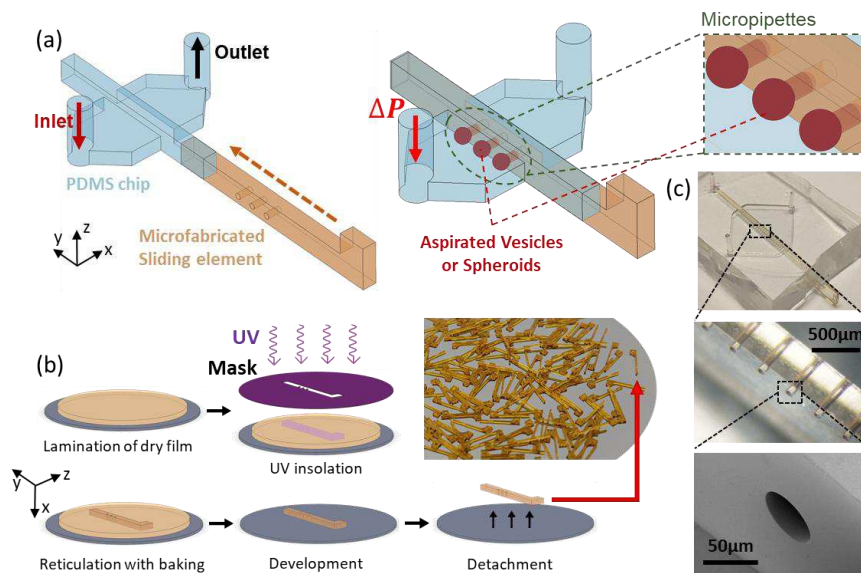
PLEASE CITE THIS ARTICLE AS DOI: 10.1063/1.5019333

88 Pipettes are designed and patterned by photolithography perpendicularly to the fabrication  
 89 plane of the channel in which they are inserted (see Figure 1). In this way, the objects injected  
 90 in a microchannel can be blocked by pipettes of a chosen shape: a circular cross-section permits  
 91 quantitative measurements analyzed with classical models, since deformations occur like in  
 92 standard MPA. Thanks to the integration, pipettes can be operated in parallel: we demonstrate  
 93 it for 7 GUVs, and up to 23 spheroids. The throughput is thus multiplied by the number of  
 94 pipettes in parallel when compared to classical MPA: with the SIMPA method we achieve ~10  
 95 tests/h for GUV, and ~20 tests/h for spheroids.

96

97 In the following, we explain in the methods the design principles and fabrication technique of  
 98 the chips, as well as their fluidic operation. We then demonstrate the interest of the technology  
 99 by assessing two situations relevant to biophysics. First, we present the results obtained on  
 100 vesicles: characterization of the elastic moduli of lipid bilayers with simple composition, and  
 101 study of the influence of sugar and cholesterol on these moduli. Second, we detail the use of  
 102 the devices for 3D cellular aggregates: measurements of the surface tension and viscoelastic  
 103 characteristics, and study of the influence of molecules targeting cell-cell adhesion.

104



105

106 **Figure 1- Principle: On-chip pipettes integrated into a microfluidic chip thanks to sliding elements** - (a) Parts view: PDMS  
 107 chip and sliding element. Assembled view after insertion, schematic close-up of aspirated micro-objects (Giant Unilamellar  
 108 Vesicles or Spheroids). b) Microfabrication workflow of the sliding elements and photograph of dozens of them, manufactured  
 109 in a single batch. c) Micrographs and SEM close-ups of the pipettes integrated into the sliding elements.

110

111

112

113 **Methods**

114 The microfluidic chips consisted of two parts, see Figure 1(a). Here, we explain the main  
115 ingredients of its design, fabrication, and operation.

116 The first part is a PDMS chip, obtained by standard soft lithography. PDMS was cast and cured  
117 on a two-level mold patterned in a photosensitive dry film (SU-8), preferred to liquid  
118 photoresist since the thickness is as high as ~500  $\mu\text{m}$ . After unmolding, holes were punched in  
119 PDMS for fluidic access.

120 The first level of the mold corresponds to the main fluidic channel, see Figure 1(a). Its height  
121 is slightly superior to the maximum diameter of the objects to be probed with pipettes, typically  
122 ~100  $\mu\text{m}$  for studies on vesicles, and ~450  $\mu\text{m}$  for spheroids.

123 The fluidic configuration is quite simple with 1 input and 1 output, the channel just getting  
124 wider at the location of sliding element insertion, to permit objects to be trapped in parallel.  
125 Note however that the design can be complexified for additional functions: we demonstrate for  
126 instance injection of a chemical stimulus around spheroids, thanks to extra lateral channels (see  
127 Figure SI-8).

128 The fluidic channel is intersected by another guide, integrated in the second layer of the mold,  
129 which is open to the outside. Its purpose is to accommodate the sliding element integrating the  
130 pipettes, the second part that composes our chips.

131 The PDMS part was then bonded by plasma on a thin layer of PDMS (50  $\mu\text{m}$ ), compromising  
132 between optical access for microscopy and deformation to avoid leakage.

133 The second element is the sliding element containing the pipettes to be integrated into the fluidic  
134 channel by insertion in the PDMS chip. This long parallelepiped including holes that constitute  
135 the pipettes was manufactured by photolithography using the same type of dry film, see Figure  
136 1(b). After optimizing fabrication parameters, we obtained pipettes with an aspect ratio up to  
137 20 (25  $\mu\text{m}$  diameter for 500  $\mu\text{m}$  length) and with a low roughness: typically, only a few ~20  
138 nm-high asperities can be seen inside the pipette, as shown in Figure 1(c) and Figure SI-1. For  
139 pipettes with lower diameters (down to 12  $\mu\text{m}$  for GUVs, see Figure 2(a), and 5  $\mu\text{m}$  for single  
140 cells), a multi-layer lamination protocol was used. Lamination was realized on a sacrificial layer  
141 (copper-titanium alloy), chemically etched after fabrication to release the sliding elements from  
142 the wafer. Since fabrication was realized by batches on a 4-inch wafer, up to 150 reusable SMPs  
143 (sliding micropipettes) could be obtained in a single fabrication run, which took a few hours.

144 Integration was made by inserting the SMP in the PDMS chip. This step could be achieved in  
145 a few minutes, either manually under a binocular microscope, with alignment precision between  
146 the pipettes and the fluidic channel in the order of 50  $\mu\text{m}$ , or aided by a specific 3D-printed  
147 holder if better alignment was required (see Figure SI-2). To reduce friction, an anti-adhesive  
148 coating (fluorinated silane deposited in the gas phase) was realized on the SMPs before  
149 insertion. Insertion was also facilitated thanks to isopropanol lubrication, eliminated afterward  
150 by evaporation (see Supplementary Information).

151 Once inserted, the SMP blocked the fluid in the main channel by letting it flow only through its  
152 cylindrical holes. The height and width of the guide were 20% smaller than the height and width  
153 of the sliding element it received (typically 450  $\mu\text{m}$  for the guide and 550  $\mu\text{m}$  for the sliding  
154 element), which we found optimum for elastic deformation to ensure a good sealing upon  
155 insertion. We checked the absence of leakage in the whole range of the pressure controller (325  
156 mbar). Thus, when a vesicle or a spheroid was injected into the inlet solution, it was carried by

157 the flow until it arrived in front of one of the micropipettes into which it was blocked and  
 158 aspirated. In the design of the SMPs, the center of the pipette was placed at a Z position  
 159 permitting objects to be trapped without touching the bottom of the fluidic channel, while being  
 160 in focus under the microscope.

161 Chip operation differed slightly for GUVs and spheroids and are detailed in the next sections  
 162 and the Supplementary Information. Fluidic protocols shared some characteristics: after  
 163 degassing and injection of the buffer to pre-wet the whole chip, the solution containing the  
 164 objects of interest was injected to trap them at the pipettes. Measurements of the mechanical  
 165 properties were achieved by quantifying deformations (of the GUVs or spheroids) under a  
 166 programmed pressure sequence, by optical microscopy and image analysis. Since the hydraulic  
 167 resistance of the pipettes was much larger than those of the inlet and outlet channels, the  
 168 pressure drop  $\Delta P$  applied to vesicles or spheroids was almost equal to the pressure drop applied  
 169 on the whole channel  $\Delta P_{channel}$ , even in the case where some pipettes were not blocked.

170 This fabrication approach permitted the integration of cylindrical holes (or any extruded shape  
 171 of arbitrary cross-section) aligned with the main axis of fluidic channels, thanks to the  
 172 photolithography of two elements along two orthogonal planes, which can hardly be achieved  
 173 by standard manufacturing techniques. This feature makes SIMPA technology uniquely suited  
 174 for high throughput micropipette aspiration, which we demonstrate in the following sections.

175

### 176 **Micropipettes for vesicles: elastic moduli of lipid membranes**

177 The mechanics of a lipid bilayer can be described by two main parameters: its resistance to  
 178 bending, quantified by the bending modulus  $\kappa_c$ ; and its resistance to an increase of area per  
 179 molecule (stretching modulus  $K_A$ ). These moduli determine how the area of a vesicle  $A$   
 180 increases with its tension  $\sigma$ , with reference to a state at low tension  $A_0, \sigma_0$ . The relative area  
 181 increase,  $\alpha = (A - A_0)/A_0$ , reads <sup>7,12</sup>:

$$182 \quad \alpha = \frac{k_B T}{8\pi\kappa_c} \ln(1 + \sigma/\sigma_0) + (\sigma - \sigma_0)/K_A, \quad (1)$$

183 where  $k_B$  is the Boltzmann constant, and  $T$  the temperature.

184 The increase of area at low tension is mostly controlled by the smoothing of thermal fluctuations  
 185 against bending (first term of equation (1)), whereas for a higher tension (typically 1 mN/m), it  
 186 is set by the stretching modulus  $K_A$  (second term of equation (1)).

187 In standard micropipette experiments, a progressively increasing tension is induced thanks to a  
 188 pressure difference  $\Delta P$  applied to the vesicle aspirated in the pipette. With the hypothesis that  
 189 the pressure inside the vesicle is equilibrated, and that the tension is homogeneous, the vesicle  
 190 tension can be deduced from Laplace law according to:

$$191 \quad \sigma = \frac{\Delta P \cdot D_p}{4(1 - D_p/D_v)}, \quad (2)$$

192 where  $D_p$  and  $D_v$  are the pipette and vesicle diameters, respectively. With the additional  
 193 hypothesis of constant vesicle volume during the experiment (low permeability of the lipid  
 194 bilayer to solvent, few minutes experiments duration), and a first-order approximation  
 195 ( $D_p^2 \Delta L_p \ll D_v^3$ ), the area increase is deduced from  $\Delta L_p$ , the position of the vesicle protrusion  
 196 within the pipette with respect to the reference state ( $A_0, \sigma_0$ ), see Figure 2(b):

$$197 \quad \Delta A = \pi D_p \Delta L_p \left(1 - \frac{D_p}{D_v}\right). \quad (3)$$



This is the author's peer reviewed, accepted manuscript. However, the online version of record will be different from this version once it has been copyedited and typeset.

PLEASE CITE THIS ARTICLE AS DOI: 10.1063/1.5019333

198 These principles apply to our microfluidic chips: we designed channels (100  $\mu\text{m}$  deep, 400  $\mu\text{m}$   
 199 wide) in which fluorescently labeled GUVs with a typical diameter of 50  $\mu\text{m}$ , obtained by  
 200 standard electroformation (see Supplementary Information), could flow. The channels  
 201 integrated sliding elements with up to 7 pipettes of diameter  $D_p \approx 12 \mu\text{m}$ , see Figure 2(a). The  
 202 pressure was slowly increased by steps (3 s duration), to quantify the increase of  $L_p$  with  $\Delta P$ ,  
 203 see Figure 2(b). The first step leading to a measurable GUV deformation was used as the  
 204 reference state ( $\Delta P_0, \Delta L_p = 0, A_0, \sigma_0$ ), see the top panel in Figure 2(b).

205 For large enough GUVs ( $D_v \geq 2.5D_p$ ), standard image analysis was used to deduce  $\Delta L_p$  as a  
 206 function of  $\Delta P$ . The relative area increase as a function of the tension was then calculated from  
 207 Equations (2)-(3) for each GUV. The values of the bending and stretching moduli were then  
 208 deduced by fitting Equation (1) to the experimental curve. As exemplified in Figure 2c showing  
 209 six measurements realized in parallel, we have used a three-parameter fit, by letting the  
 210 reference tension as a free parameter, in addition to the determination of  $\kappa_c$  and  $K_A$ . It was found  
 211 to reproduce more accurately the data trend in the bending regime than a two-parameter fit and  
 212 fixed experimental reference tension  $\sigma_{0exp}$ . The associated difference between  $\sigma_{0exp}$  and the  
 213 fitted value was in the range  $\delta\sigma_0 \leq 10^{-5} \text{ mN/m}$ , corresponding to a pressure difference  $\delta P \leq$   
 214 3 Pa. We independently characterized the accuracy of pressure control to be better than 0.5 Pa,  
 215 so this value is a little higher than expected. We attribute this slight discrepancy to higher  
 216 uncertainty in determining the absolute value of the pressure, even though relative variations  
 217 are precisely measured. With this procedure, the curve superimposed on experimental data both  
 218 for bending and stretching regime, with a coefficient of determination of the fitting  $R^2 \geq 0.99$ .

219  
 220  
 221  
 222  
 223  
 224  
 225  
 226  
 227  
 228

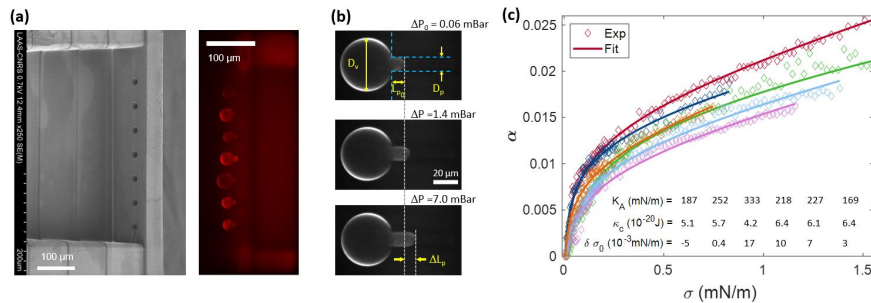


Figure 2- On-chip pipettes applied to Giant Unilamellar Vesicles to quantify the mechanics of lipid membranes (bending and stretching moduli). (a) SEM image of a sliding element with a design adapted to GUVs, including 7 pipettes (12  $\mu\text{m}$  in diameter), and fluorescence microscopy micrograph of 7 DOPC GUVs trapped within such pipettes inserted in a PDMS channel. (b) Fluorescence micrographs of a GUV blocked inside a 12- $\mu\text{m}$ -diameter pipette, for three values of the pressure difference applied to the vesicle. Reference situation  $\Delta P_0$ , and two successive equilibrium positions. The quasistatic increase of pressure causes a progressive increase of the GUV area, quantified from the length of the GUV protrusion within the pipette. (c) Evolution of the relative area increase as a function of the tension for six DOPC GUVs of the same experimental run, and fitted curve according to equation (1). The displayed numbers correspond to the outcomes of the fitting for this particular experiment, as a typical example of data dispersion.

### 229 Results for GUVs of simple composition and effects of sugar and cholesterol

230 The results obtained with GUVs of simple composition (bilayer of the mono-unsaturated lipids  
 231 1,2-dioleoyl-sn-glycero-3-phosphocholine, DOPC in sucrose solutions) are summarized in the  
 232 histograms of Figure 3(a). The statistics are slightly lower for the stretching modulus  $K_A$  ( $N =$   
 233 41) than for the bending modulus  $\kappa_c$  ( $N = 59$ ) because some GUVs escaped the pipettes at  
 234 moderate pressure, without fully entering the stretching regime. We deduced the value of  $K_A$   
 235 only for vesicles escaping at a tension  $\sigma \geq 0.75 \text{ mN/m}$ . This fragility, which can be attributed

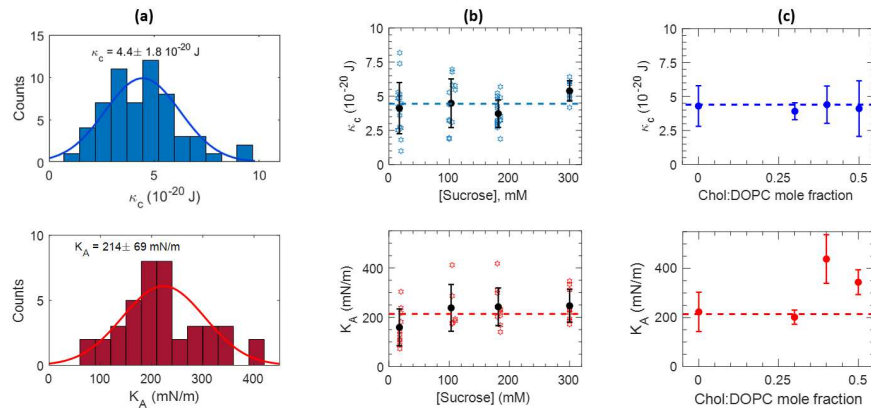
This is the author's peer reviewed, accepted manuscript. However, the online version of record will be different from this version once it has been copyedited and typeset.

PLEASE CITE THIS ARTICLE AS DOI: 10.1063/1.5019333

236 to dispersion in the lysis tension, possibly due to minor defects in some GUVs, was not  
 237 correlated to the measured value of  $K_A$  and  $\kappa_c$ .

238 We also investigated the effect of the sucrose concentration on the bilayer mechanics, for DOPC  
 239 lipids, see Figure 3(b). No systematic variation of both bending and stretching moduli was  
 240 observed from 15mM to 300 mM, within our experimental error.

241 Finally, we performed measurements on bilayers composed of DOPC mixed with up to 50%  
 242 cholesterol, Figure 3(c). We observed no dependence of the bending modulus on the  
 243 cholesterol/lipid molar fraction, whereas the stretching modulus almost doubled for molar  
 244 fractions 0.4 and 0.5.



245 Figure 3- Bending and stretching moduli of lipid bilayers. (a) Histograms of the bending (top) and stretching (bottom)  
 246 moduli of DOPC membranes, and associated Gaussian fits. (b) Influence of the sucrose concentration on the value of the bending (top)  
 247 and stretching (bottom) moduli, for DOPC membranes. (c) Influence of cholesterol on the bending (top) and stretching (bottom)  
 248 moduli of mixed DOPC-cholesterol vesicles, as a function of the cholesterol:DOPC mole fraction.  
 249

250 *Discussion: on-chip pipette to characterize vesicle mechanics*

251 Overall, the results in Figure 2 and Figure 3 show that the proposed approach is suited to  
 252 determine the mechanical properties of lipid membranes, similar to the classical micropipette  
 253 aspiration. However, the throughput of our method is higher (roughly multiplied by the number  
 254 of pipettes in parallel, 7 in Figure 2) since several GUVs can be characterized in parallel. The  
 255 integration in a microfluidic device has also the advantage of avoiding the manual search of  
 256 vesicle and micromanipulation of the pipette, since the driving flow in the channel naturally  
 257 brings the vesicles to the pipettes, and facilitates the trapping of GUVs. In addition, pressure  
 258 controllers used in routine microfluidic setups have sub-second response time and permit the  
 259 automation of pressure vs. time protocols.

260 The obtained values are reasonably consistent with the literature. For DOPC at room  
 261 temperature, the determined stretching modulus  $K_A = 214 \pm 69$  mN/m falls within the range  
 262 of most micropipette measurements (respectively  $K_A = 210 \pm 25$  mN/m, 198 mN/  
 263 m, and  $265 \pm 18$  mN/m for references <sup>26-28</sup>). The bending modulus we obtained ( $\kappa_c =$   
 264  $4,4 \pm 1,8 \cdot 10^{-20}$  J) is in the lower limit of published values for measurements with  
 265 micropipettes (respectively  $\kappa_c \sim 9,1 \pm 1,5 \cdot 10^{-20}$  J,  $8,5 \cdot 10^{-20}$  J,  $4,7 \cdot 10^{-20}$  J for DOPC in  
 266 references <sup>26,28,29</sup>), reported in a recent review <sup>30</sup> to be in the range  $\kappa_c = 4 - 16 \cdot 10^{-20}$  J for  
 267 monounsaturated lipids. It has to be mentioned that systematic differences between groups and



This is the author's peer reviewed, accepted manuscript. However, the online version of record will be different from this version once it has been copyedited and typeset.

PLEASE CITE THIS ARTICLE AS DOI: 10.1063/1.5019333

268 measurement method are thoroughly discussed, and only partly explained by differences in the  
269 probes scales or experimental protocols, in several reviews<sup>7,30-32</sup>.

270 The dispersion of our data is a bit higher than in the literature (coefficients of variation 41%  
271 and 29% for  $\kappa_c$  and  $K_A$  respectively). GUVs synthesized via electroformation have inherent  
272 variability. We also attribute the dispersion to the fact that the only eliminated GUVs were those  
273 with diameter  $D_v \leq 2.5D_p$ ), or with visible defects (such as internal vesicles), contrary to  
274 standard micropipette aspiration where the operator arbitrarily chooses the GUV to be probed.

275 The absence of influence of sugar concentration we observed (Figure 3(b)) is consistent with  
276 most recent observations and discussions of the literature, even though this is still a quite  
277 controversial issue.<sup>32-35</sup>

278 When varying the membrane composition by mixing DOPC with cholesterol, we observed no  
279 change in the bending modulus, from pure DOPC up to the maximum cholesterol content tested  
280 (0.5mol/mol). On the opposite, a two-fold increase was observed for  $K_A$  for increasing  
281 cholesterol content, with a possible threshold between 0.3 and 0.4 molar fraction in cholesterol.  
282 These observations complete a rich literature on the issue of cholesterol's influence on  
283 membrane structure and properties. Bending rigidity was shown to be strongly lipid  
284 dependent<sup>36,37</sup>, stiffening by cholesterol being observed only for saturated lipids, with no effect  
285 for mono-unsaturated lipids such as the DOPC used in the present study<sup>38,39</sup>, or even slight  
286 softening related to coupling between bending and cholesterol localization<sup>40</sup>.

287 Finally, changing the chip design permits controlling physico-chemical stimuli around trapped  
288 objects. Pipettes including slits to let a fraction of the flow pass can be used to probe vesicles  
289 while submitted to shear stress: by using cross-shaped pipettes, we have observed that shear  
290 stress affects lipid domains, as demonstrated in reference<sup>41</sup>, see Figure SI-7. Since a  
291 microfluidic lateral channel can be integrated into the design, the approach is well-suited for  
292 temporal change of the chemical environment surrounding the GUVs. It opens interesting  
293 perspectives to investigate for example the kinetics of the interaction of lipid bilayers with  
294 biomolecules or relevant synthetic entities (molecules, macromolecules, or nanosystems).

295

### 296 **Micropipettes on cell aggregates: quantifying spheroids' rheology**

297 Many biological tissues behave as viscoelastic fluids, which is both due to the properties of  
298 individual cells (cytoskeleton, nucleus), and to the way they assemble in the tissue (extracellular  
299 matrix, adhesion between cells). Thus, when a spheroid (simple 3D cell aggregate) is probed  
300 by micropipette aspiration with a pressure step, it reacts with two different regimes. First, an  
301 instantaneous deformation is observed, directly linked to the tissue's elastic properties. Then,  
302 over time, the tissue flows into the micropipette like a viscous fluid. Several viscoelastic models  
303 describe this type of material, but the modified Kelvin-Voigt shown in the insert of Figure 4(b)  
304 is the simplest that closely reproduces the response observed in Figure 4(b). It consists of a  
305 Kelvin-Voigt element (spring  $k_1$  in parallel with damper  $\mu_c$ ), modified by the spring  $k_2$  to  
306 account for an instantaneous elastic response, in series with a dashpot  $\mu_t$ , which corresponds to  
307 long-term viscous flow. In this description of the tissue as a soft material, viscosity and  
308 elasticity are completed by the aggregate's surface tension  $\gamma$ , excess of surface energy that  
309 originates from a combination of the interaction between cells, and differences in cortical  
310 tension between the peripheric and the core cells<sup>10,42</sup>. In a standard micropipette experiment, a  
311 spheroid of radius  $R$  is aspirated in a pipette of radius  $R_p$  with a suction pressure  $\Delta P$ . The  
312 effective force inducing spheroid deformation reads:  $f = \pi R_p^2(\Delta P - \Delta P_c)$ , where  $\Delta P_c =$

This is the author's peer reviewed, accepted manuscript. However, the online version of record will be different from this version once it has been copyedited and typeset.

PLEASE CITE THIS ARTICLE AS DOI: 10.1063/1.5019333

313  $2\gamma\left(\frac{1}{R_p} - \frac{1}{R}\right)$  is the Laplace pressure generated by the curvature imposed by the pipette.  $\Delta P_c$   
 314 corresponds to the minimum pressure needed for the spheroid to continuously flow inside the  
 315 pipette. For  $\Delta P > \Delta P_c$ , the spheroid's response to a differential pressure step can be written, in  
 316 terms of its temporal elongation  $L(t)$  inside the pipette (see Figure 4(a)):

$$317 \quad L(t) = \frac{f}{k_1} \left( 1 - \frac{k_2}{k_1 + k_2} e^{-\frac{t}{\tau_c}} \right) + \frac{f}{\mu_t} t, \quad (4)$$

318 where  $\tau_c = \frac{\mu_c(k_1 + k_2)}{k_1 k_2}$  is a viscoelastic characteristic time.

319 The first term in equation (4) refers to a viscoelastic solid, with two elastic moduli acting at two  
 320 timescales: a first modulus  $E_i = (k_1 + k_2)/\pi R_p$ , associated with an instantaneous deformation  
 321 of the spheroid, and a second elastic modulus  $E = k_1/\pi R_p$ , which comes into play after a  
 322 typical time  $\tau_c$ . These two elastic moduli are usually attributed to the cellular cytoskeleton's  
 323 reaction to pressure: the elasticity of the actin cortex is first assessed, fibers then rearrange,  
 324 leading to a softer long-time elastic response.

325 The second term describes flow at the tissue level and it corresponds to the constant speed flow  
 326 of a fluid of viscosity  $\eta = \mu_t/3\pi^2 R_p$  inside the pipette, with the hypothesis that viscous  
 327 dissipation occurs only at the inlet, due to cell rearrangements. As detailed in reference<sup>14</sup>, this  
 328 regime neglects wall friction, which is achieved thanks to surface treatment limiting cell  
 329 adhesion on the pipette's walls.

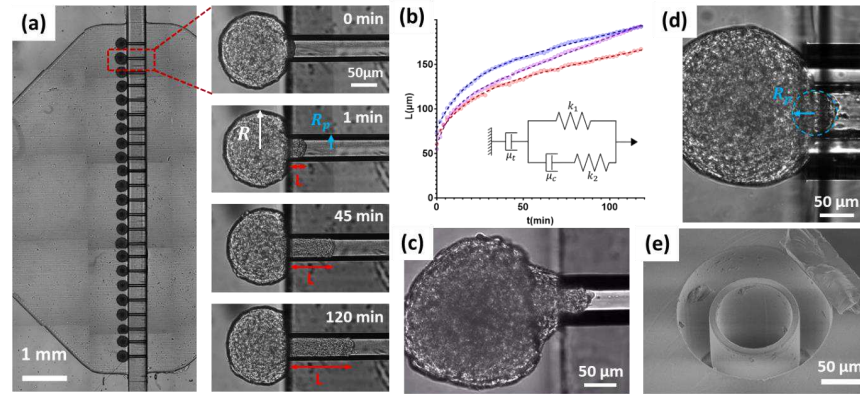
330 It is worth noting that these quantitative relationships between the Kelvin-Voigt parameters  
 331  $(k_1, k_2, \mu_t)$  and the macroscopic viscoelastic moduli  $(E_i, E, \eta)$  slightly depends on the thickness  
 332 of the pipette wall. They are correct for our SIMPA configuration (thick walls), whereas they  
 333 need to be corrected by a few percent for classical MPA (thin walls), as discussed in references  
 334<sup>43</sup> and<sup>44</sup> regarding elasticity and viscosity, respectively.

335 We have developed microfluidic chips enabling parallel aspiration of up to 23 spheroids, see  
 336 Figure 4(a). The channel height was 450  $\mu\text{m}$  to accommodate all spheroid sizes. The chamber  
 337 width was 10 mm for the 23-position chip (2 mm for the 5-position chip). A single  
 338 microfabrication run allowed us to manufacture around 150 SMPs, see photo in Figure 1(b),  
 339 which permitted us to test different pipette diameters and designs. Most experiments were  
 340 conducted with 70  $\mu\text{m}$  diameter pipettes, chosen as a compromise: much smaller than spheroids  
 341 size, and significantly larger than cells size, for the granular nature of the tissue not to be too  
 342 critical for the continuous description of the rheological model. Pipettes were 500  $\mu\text{m}$  in length.  
 343 A pressure step was applied to the spheroids, as detailed in the Supplementary Information. As  
 344 mentioned in the Methods, the total channel pressure drop would be exerted on the pipettes  
 345 even without spheroids blocking all of them, because they dominate the chip's hydraulic  
 346 resistance. However, we only conducted experiments in which one spheroid is present in each  
 347 pipette, to avoid the flow of buffer in free pipettes, that could affect the overall pressure  
 348 difference because of a hydrostatic contribution upon increase of the outlet reservoir level.

This is the author's peer reviewed, accepted manuscript. However, the online version of record will be different from this version once it has been copyedited and typeset.

PLEASE CITE THIS ARTICLE AS DOI: 10.1063/5.0193333

349  
350  
351  
352  
353  
354  
355  
356  
357



358  
359  
360  
361  
362  
363  
364  
365  
366  
367  
368  
369

370  
371  
372  
373  
374  
375

376  
377  
378  
379  
380  
381  
382  
383

Figure 4- On-chip pipettes applied to 3D cellular aggregates to quantify their viscosity and elasticity. (a) Micrograph of 23 spheroids trapped in the pipettes in the SIMPA chip. Close-up on a single micropipette: time-lapse of the aspiration of one A338 spheroid submitted to a pressure step  $\Delta P = 50$  mbar from  $t = 0$  s. (b) Evolution of the spheroids' positions  $L(t)$  in the pipette as a function of time for 3 simultaneous parallel measurements, and fitted curves according to equation (4). (c) Micrograph of a spheroid just after release of the aspiration pressure. The conical shape indicates that Laplace pressure is not the only process expelling the spheroid from the pipette, during retraction. (d) Micrograph of a spheroid aspirated with a pressure just equal to the Laplace pressure  $\Delta P_c$ , leading to a radius equal to the pipette's radius. (e) SEM image of the pipette design with a thin wall, used to improve the optical quality of the image in (d).

To validate quantitatively the SIMPA approach with respect to MPA, we performed measurements on the murine sarcoma cell line S180-GFP that was characterized by Guevorkian *et al.*<sup>13</sup> by MPA. Since Laplace pressure contributes to the spheroid's flow (see Equation (4)), the surface tension  $\gamma$  needs to be determined to deduce the viscoelastic parameters. Like in reference<sup>13</sup>, aspiration was followed by retraction experiments, in which Laplace pressure is the only source of movement. The histograms of measured viscoelastic parameters are plotted in Figure SI-4 ( $N = 23$ ). We obtained  $\gamma = 10.8 \pm 2.4$  mN/m,  $\eta = 1.37 \pm 0.03 \cdot 10^5$  Pa. s,  $E = 213 \pm 17$  Pa,  $E_i = 773 \pm 47$  Pa. The values of the viscosity and long-time elasticity are fully consistent with the results reported in reference<sup>13</sup> ( $\eta = 1.9 \pm 0.3 \cdot 10^5$  Pa. s, elastic modulus deduced from an average of relaxation times:  $E = 700 \pm 100$  Pa), given that the cell line may have slightly evolved since 2010, and more importantly that the culture conditions to form the spheroids were not exactly the same in the two studies.

For A338 mouse pancreatic cancer cell spheroids, a typical timelapse for one position is shown on the right panel of Figure 4(a), and in Supplementary Video 1. The position of the spheroid protrusion as a function of time  $L(t)$  was determined by a custom image segmentation algorithm described in Supplementary Information, see Figure SI-5 and Supplementary Video 3. Typical results of a single experiment driven on A338 spheroids are displayed in Figure 4(b), together with the fit of these results by equation (4).

However, regarding surface tension, we observed for this cell line a complex conical shape of the spheroid upon retraction, see Figure 4(c) and Supplementary Video 2, and its fast ejection from the pipette. Several mechanisms could explain this behavior: stored elastic energy could contribute to expelling the spheroid out of the pipette (similarly to what is mentioned in reference<sup>18</sup>), and additionally thanks to low wall friction the spheroid could slide upstream without dissipation and progressively round up at the pipette's corner because of surface tension. We thus used alternatives to such retraction experiments and measured  $\gamma$  by directly characterizing Laplace pressure thanks to other sets of experiments. We quantified the

This is the author's peer reviewed, accepted manuscript. However, the online version of record will be different from this version once it has been copyedited and typeset.

PLEASE CITE THIS ARTICLE AS DOI: 10.1063/1.5019333

384 minimum critical pressure leading to continuous flow of the spheroid  $\Delta P_{crit}$ , which should also  
385 correspond to the pressure for which the radius of the spheroid meniscus (formed by cells at its  
386 surface within the pipette) equals the pipette radius, see Figure 4(d). This set of experiments  
387 was realized on a specially designed thin-wall pipette, see Figure 4(e), to improve the quality  
388 of optics. Both pressures were determined to be very close and equal to  $\Delta P_{c-crit} = 5 \pm$   
389  $0.5$  mbar). These measurements led to a value of the surface tension  $\gamma_{crit} = 10 \pm 1$  mN/m.  
390 We also quantified the ratio  $\gamma/\eta$  from the dynamics of spheroid fusion<sup>45</sup>, see Supplementary  
391 Information, Figure SI-6. These independent off-chip experiments led to  $\gamma_{fusion} = 4.5 \pm$   
392  $0.9$  mN/m. The fusion experiment mainly probes the external layers of the spheroid, and the  
393 surface tension of cell aggregates was recently discussed theoretically to be a multi-scale  
394 complex concept<sup>46</sup>, so that different configurations could lead to slightly different results. The  
395 viscosity retained for this fitting was the one deduced from aspiration experiments. In addition,  
396 note that in both cases, the value corresponds to the surface tension at low stress, referred to as  
397  $\gamma_0$  in previous studies which have evidenced a possible increase of  $\gamma$  upon aspiration<sup>13</sup>. We  
398 finally retained the on-chip measured value  $\gamma_{crit}$ , since it was determined in the same flow  
399 configuration as the pipette aspiration. It is in the typical range of literature measurement of  
400 biological tissues' surface tension<sup>47</sup>, even though most available data are on less cohesive  
401 configurations than the epithelial one probed here. Let us mention that since the applied  
402 pressure in aspiration experiments was significantly higher than the typical Laplace pressure,  
403 an error in surface tension determination would not critically affect the determination of  
404 viscoelastic parameters.

405 With this value of the surface tension, we extracted the rheological parameters from the fitting  
406 of the experimental curves  $L(t)$  with equation (4), see Figure 4(b). The fittings closely  
407 reproduced the trends of the experiments. Graphically, tissue viscosity is deduced from the  
408 slope at a long time, whereas the first (short-time) elastic modulus  $E_i$  can be deduced from the  
409 initial instantaneous elongation of the spheroid, the second modulus  $E$  from the intercept of the  
410 long-time linear flow regime with the vertical axis, and  $\tau_c$  from the typical time scale to reach  
411 this regime.

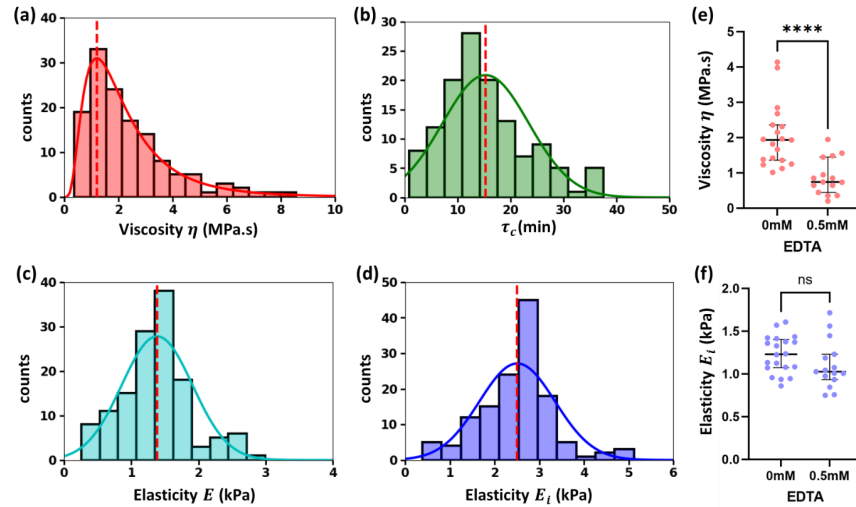
412

#### 413 *Measuring viscoelastic properties of spheroids: results and discussion.*

414 The results obtained with A338 spheroids are shown in Figure 5(a). All ( $N = 134$ )  
415 measurements were realized with the 5-pipettes design, in about 30 experiments, each lasting a  
416 few hours, which demonstrates the high throughput of the method. We measured elastic moduli  
417  $E = 1.4 \pm 0.5$  kPa,  $E_i = 2.5 \pm 0.9$  kPa, and a time scale  $\tau_c = 15.3 \pm 8.1$  min (error bars  
418 indicates the standard deviation). For viscosity, the distribution was observed to be better fitted  
419 by a log-normal distribution than by a Gaussian. The maximum (mode) of the fitted distribution  
420 was  $\eta_{ln} = 1.20$  MPa.s, with a distribution width  $\sigma_{\eta-ln} = 0,67$  MPa.s. We observed a more  
421 reduced dispersion between spheroids of the same batch: the average of standard deviations  
422 deduced from single experiments (5 or 23 simultaneous measurements) was  $\sigma_{\eta-batch} =$   
423  $0.5$  MPa.s and  $\sigma_{E_i-batch} = 0.35$  kPa for the viscosity and short-time elasticity  $E_i$  respectively.  
424 These values can be interpreted as an upper bound of the measurement uncertainty,  
425 demonstrating the reproducibility of the technique. The width of the histograms in Figure 5(a)  
426 mostly originates from biological variability.

This is the author's peer reviewed, accepted manuscript. However, the online version of record will be different from this version once it has been copyedited and typeset.

PLEASE CITE THIS ARTICLE AS DOI: 10.1063/5.0193333



427  
428  
429  
430

Figure 5- Viscoelastic properties of A338 cellular aggregates: histograms of the viscosity (a), characteristic viscoelastic time (b), long-time elasticity (c), short-time elasticity (d). (e-f) Influence of EDTA on the spheroids' viscosity and short-time elasticity.

431 To the best of our knowledge, no viscoelastic measurements have been published for this cell  
432 line. However, the high value of viscosity and elasticity, about ten times the typical values  
433 measured for very dynamic embryonic tissues<sup>48</sup>, are consistent with the strong cohesion of  
434 pancreatic epithelial-like tissues.

435 We also assessed the effect of Ethylenediaminetetraacetic acid (EDTA). EDTA affects  
436 adhesion between cells by chelating metallic ions, including calcium, necessary for adhesion  
437 proteins to operate. We incubated the cells with EDTA during the formation of the spheroids  
438 before measuring viscoelastic properties. The results are shown in Figure 5(e-f). The viscosity  
439 was significantly reduced for spheroids incubated with EDTA with respect to the control,  
440 whereas short-time elasticity was not affected. This behavior is consistent with a reduced  
441 adhesion facilitating rearrangement of cells (T4 events<sup>21</sup>), leading to decreased viscosity,  
442 whereas elasticity, originating mostly from cells' cytoskeletons, was not strongly impacted.

443 We now discuss the specificities of the SIMPA technology for spheroid rheology, with respect  
444 to existing methods.

445 First, the approach benefits from the advantages of standard MPA: it is quantitative, and it  
446 probes optically determined locations of an object, which opens the possibility to test different  
447 zones of a tissue for non-spherical aggregate. MPA applies forces from the external cell layers,  
448 which can give complementary information to methods applying homogeneous stress, like  
449 magnetic rheometry<sup>49</sup>. In our chips, since it is the microfluidic flow that pushes the spheroids  
450 towards the pipettes, the spheroid's orientation and the precise point they contact the pipette's  
451 inlet cannot be controlled by the operator independently of the fluidic design, which can appear  
452 as a limitation. However, for non-spherical objects it could turn into an advantage: the shape of  
453 the upstream channel and the location of pipettes on the sliding element could be specifically  
454 designed to set this orientation and probe well-defined areas.

This is the author's peer reviewed, accepted manuscript. However, the online version of record will be different from this version once it has been copyedited and typeset.

PLEASE CITE THIS ARTICLE AS DOI: 10.1063/1.5019333

455 The SIMPA technology has unique features compared to standard MPA: the throughput is  
 456 multiplied by the number of spheroids that can be probed in parallel (demonstrated to be up to  
 457 23 in this article). In addition, the chip format permits the use of low volumes of sample  
 458 (typically a few hundred  $\mu\text{L}$ ), with a spontaneous spheroid loading since the flow naturally  
 459 pushes the spheroids to the free SMPs. The chips can also be washed and reused, and the  
 460 spheroids extracted out of the chip for further characterization. It is possible to keep spheroids  
 461 for long times (we observed spheroids stable for three days with no visible necrosis). This  
 462 comes from the environmental chamber surrounding the chip on the microscope (temperature  
 463 set to  $37^\circ\text{C}$  and 5%  $\text{CO}_2$ ), but also from PDMS permeability to oxygen, and from a fast diffusion  
 464 of nutrients within the chips. Finally, adding lateral fluidic channels close to the sliding element  
 465 permits changing in real time the chemical environment of trapped spheroids, see Figure SI-8.  
 466 As a proof of concept, we demonstrated the dynamic exposure of trapped spheroids to  
 467 microparticles, see Supplementary Videos 4 and 5. This type of design could be relevant to  
 468 study the response to drugs at short timescales, typically seconds or minutes. Quantifying the  
 469 influence of different drugs, at different timescales, should improve our understanding of the  
 470 microscopic origin of tissue rheology. In the same perspective, the technology can apply a  
 471 dynamic pressure stimulus, as in reference <sup>49</sup>, which is a relevant way to assess the validity of  
 472 different rheological models, or to apply spatio-temporal stimulations such as the ones  
 473 originating from heart beating or circadian cycle.

474

#### 475 **Conclusion**

476 We present in this paper the SIMPA technology, a parallel, quantitative integrated aspiration  
 477 micropipette method. We demonstrate its relevance to characterize quantitatively mechanics  
 478 both at the cell membrane scale and at the multicellular scale. With respect to standard MPA,  
 479 its throughput is multiplied by the number of pipettes in parallel, shown to be for this proof of  
 480 concept 7 and 23 for GUVs and spheroids respectively, leading to a throughput of order  $\sim 10$   
 481 tests/h for GUVs, and  $\sim 20$  tests/h for spheroids. With respect to other integrated on-chip  
 482 micropipettes<sup>18,20,21</sup>, our approach is the only one that combines circular geometry and parallel  
 483 probing, in a user-friendly format. Thus, even if interesting analyses have been developed  
 484 recently for squares or rectangles<sup>19</sup>, circular traps are quantitative by design, they fully eliminate  
 485 both anisotropy of the constraints and residual flows in the corners.

486 Several perspectives emerge from the versatility of the method, related to fluidic design. As the  
 487 most obvious evolution, larger fluidic chambers, or pipettes placed at different z-positions,  
 488 could lead to an even larger throughput by adding further parallel pipettes, if required. More  
 489 interestingly, changing the chip design permits controlling physico-chemical stimuli around  
 490 trapped objects.

491 As a further perspective, we could extend the single vesicle configuration to the probing of  
 492 single cells, by using pipettes with diameters of order  $2\text{-}5\ \mu\text{m}$ , which is fully compatible with  
 493 photolithography techniques used in this work. By providing direct measurements of  
 494 mechanical parameters, with a better throughput than conventional micropipettes, that could be  
 495 very complementary to high throughput microfluidic deformability cytometry<sup>50</sup>.

496 Finally, specific versions of the technology can be developed to improve the quality of optics  
 497 (thinner walls, see Figure 4(c), or glass versions of the sliding elements, see Supplementary  
 498 Video 6). Overall, the SIMPA technology will help identify how collective properties emerge  
 499 from individual cell deformations and rearrangements.



500 **Supplementary Material**

501 Supplementary material accompanies the manuscript on the APL Bioengineering website. It  
 502 details microfabrication protocols, preparation of GUVS, cell culture and preparation of  
 503 spheroids, and microfluidic protocols. SEM images of the pipettes are also provided (Figure SI-  
 504 1), as well as the device to control the insertion of the pipettes (Figure SI-2), and  
 505 characterization of the dry film fluorescence (Figure SI-3). Full histograms of the viscoelastic  
 506 properties are shown in Figure SI-4. Image analysis algorithm is described and exemplified in  
 507 Figure SI-5. The independent off-chip measurement of surface tension is explained and shown  
 508 in Figure SI-6. An alternative geometry enabling to expose trapped object to a fluid shear stress  
 509 is shown in Figure SI-7, together with its use to demonstrate the effect of shear on lipid domains.  
 510 Figure SI-8 shows a second alternative geometry to control the chemical microenvironment  
 511 around trapped objects. Finally, six supplementary videos are included, to exemplify the  
 512 different steps and possibilities of the pipettes. Their legends are provided at the end of the  
 513 Supplementary Material text.

514

515 **Data availability**

516 The data that support the findings of this study are available from the corresponding author  
 517 upon reasonable request.

518

519 **References**

- 520 1. Diz-Muñoz, A., Weiner, O. D. & Fletcher, D. A. In pursuit of the mechanics that shape cell  
 521 surfaces. *Nat. Phys.* **14**, 648–652 (2018).  
 522 2. Petridou, N. I. & Heisenberg, C.-P. Tissue rheology in embryonic organization. *EMBO J.*  
 523 **38**, e102497 (2019).  
 524 3. Lenne, P.-F. & Trivedi, V. Sculpting tissues by phase transitions. *Nat. Commun.* **13**, 664  
 525 (2022).  
 526 4. Oswald, L., Grosser, S., Smith, D. M. & Käs, J. A. Jamming transitions in cancer. *J. Phys.*  
 527 *Appl. Phys.* **50**, 483001 (2017).  
 528 5. Deptuła, P. *et al.* Tissue Rheology as a Possible Complementary Procedure to Advance  
 529 Histological Diagnosis of Colon Cancer. *ACS Biomater. Sci. Eng.* **6**, 5620–5631 (2020).  
 530 6. Gottheil, P. *et al.* State of Cell Unjamming Correlates with Distant Metastasis in Cancer  
 531 Patients. *Phys. Rev. X* **13**, 031003 (2023).  
 532 7. Bassereau, P., Sorre, B. & Lévy, A. Bending lipid membranes: Experiments after W.  
 533 Helfrich's model. *Adv. Colloid Interface Sci.* **208**, 47–57 (2014).  
 534 8. González-Bermúdez, B., Guinea, G. V. & Plaza, G. R. Advances in Micropipette Aspiration:  
 535 Applications in Cell Biomechanics, Models, and Extended Studies. *Biophys. J.* **116**, 587–  
 536 594 (2019).  
 537 9. Gonzalez-Rodriguez, D., Guevorkian, K., Douezan, S. & Brochard-Wyart, F. Soft Matter  
 538 Models of Developing Tissues and Tumors. *Science* **338**, 910–917 (2012).  
 539 10. Steinberg, M. S. Reconstruction of Tissues by Dissociated Cells. *Science* **141**, 401–408  
 540 (1963).  
 541 11. Chotard-Ghodsni, R. & Verdier, C. Rheology of Living Materials. in *Modeling of*  
 542 *Biological Materials* (eds. Mollica, F., Preziosi, L. & Rajagopal, K. R.) 1–31 (Birkhäuser  
 543 Boston, Boston, MA, 2007). doi:10.1007/978-0-8176-4411-6\_1.  
 544 12. Evans, E. & Rawicz, W. Entropy-driven tension and bending elasticity in condensed-  
 545 fluid membranes. *Phys. Rev. Lett.* **64**, 2094–2097 (1990).

This is the author's peer reviewed, accepted manuscript. However, the online version of record will be different from this version once it has been copyedited and typeset.

PLEASE CITE THIS ARTICLE AS DOI: 10.1063/5.0193333

- 546 13. Guevorkian, K., Colbert, M.-J., Durth, M., Dufour, S. & Brochard-Wyart, F. Aspiration  
547 of Biological Viscoelastic Drops. *Phys. Rev. Lett.* **104**, 218101 (2010).  
548  
549 14. Guevorkian, K., Brochard-Wyart, F. & Gonzalez-Rodriguez, D. Chapter eight - Flow  
550 dynamics of 3D multicellular systems into capillaries. in *Viscoelasticity and Collective Cell*  
551 *Migration* (eds. Pajic-Lijakovic, I. & Barriga, E. H.) 193–223 (Academic Press, 2021).  
552 doi:10.1016/B978-0-12-820310-1.00008-2.  
553 15. Guevorkian, K. & Maître, J.-L. Micropipette aspiration. in *Methods in Cell Biology* vol.  
554 139 187–201 (Elsevier, 2017).  
555 16. Lee, L. M. & Liu, A. P. A microfluidic pipette array for mechanophenotyping of cancer  
556 cells and mechanical gating of mechanosensitive channels. *Lab. Chip* **15**, 264–273 (2014).  
557 17. Elias, M. *et al.* Microfluidic characterization of biomimetic membrane mechanics with  
558 an on-chip micropipette. *Micro Nano Eng.* **8**, 100064 (2020).  
559 18. Boot, R. C. *et al.* High-throughput mechanophenotyping of multicellular spheroids  
560 using a microfluidic micropipette aspiration chip. *Lab. Chip* **23**, 1768–1778 (2023).  
561 19. Moore, C. P., Husson, J., Boudaoud, A., Amselem, G. & Baroud, C. N. Clogging of a  
562 Rectangular Slit by a Spherical Soft Particle. *Phys. Rev. Lett.* **130**, 064001 (2023).  
563 20. Davidson, P. M. *et al.* High-throughput microfluidic micropipette aspiration device to  
564 probe time-scale dependent nuclear mechanics in intact cells. *Lab. Chip* **19**, 3652–3663  
565 (2019).  
566 21. Tlili, S. L., Graner, F. & Delanoë-Ayari, H. A microfluidic platform to investigate the  
567 role of mechanical constraints on tissue reorganization. *Development* **149**, dev200774  
568 (2022).  
569 22. Layachi, M., Casas-Ferrer, L., Massiera, G. & Casanellas, L. Rheology of vesicle  
570 prototissues: A microfluidic approach. *Front. Phys.* **10**, (2022).  
571 23. Panhwar, M. H. *et al.* High-throughput cell and spheroid mechanics in virtual fluidic  
572 channels. *Nat. Commun.* **11**, 2190 (2020).  
573 24. Venzac, B. *et al.* Sliding walls: a new paradigm for fluidic actuation and protocol  
574 implementation in microfluidics. *Microsyst. Nanoeng.* **6**, 1–10 (2020).  
575 25. Meriem, Z. B. *et al.* A microfluidic mechano-chemostat for tissues and organisms  
576 reveals that confined growth is accompanied with increased macromolecular crowding. *Lab.*  
577 *Chip* (2023) doi:10.1039/D3LC00313B.  
578 26. Lu, L., Doak, W. J., Schertzer, J. W. & Chiarot, P. R. Membrane mechanical properties  
579 of synthetic asymmetric phospholipid vesicles. *Soft Matter* **12**, 7521–7528 (2016).  
580 27. Chen, D. & Santore, M. M. Hybrid copolymer–phospholipid vesicles: phase separation  
581 resembling mixed phospholipid lamellae, but with mechanical stability and control. *Soft*  
582 *Matter* **11**, 2617–2626 (2015).  
583 28. Rawicz, W., Olbrich, K. C., McIntosh, T., Needham, D. & Evans, E. Effect of Chain  
584 Length and Unsaturation on Elasticity of Lipid Bilayers. *Biophys. J.* **79**, 328–339 (2000).  
585 29. Shchelokovskyy, P., Tristram-Nagle, S. & Dimova, R. Effect of the HIV-1 fusion  
586 peptide on the mechanical properties and leaflet coupling of lipid bilayers. *New J. Phys.* **13**,  
587 025004 (2011).  
588 30. Boichichio, D. & Monticelli, L. Chapter Five - The Membrane Bending Modulus in  
589 Experiments and Simulations: A Puzzling Picture. in *Advances in Biomembranes and Lipid*  
590 *Self-Assembly* (eds. Iglíč, A., Kulkarni, C. V. & Rappolt, M.) vol. 23 117–143 (Academic  
591 Press, 2016).  
592 31. Nagle, J. F. Introductory Lecture: Basic quantities in model biomembranes. *Faraday*  
593 *Discuss.* **161**, 11–29 (2013).  
594 32. Nagle, J. F., Jablin, M. S., Tristram-Nagle, S. & Akabori, K. What are the true values of  
595 the bending modulus of simple lipid bilayers? *Chem. Phys. Lipids* **185**, 3–10 (2015).  
596 33. Vitkova, V., Genova, J., Mitov, M. D. & Bivas, I. Sugars in the Aqueous Phase Change  
597 the Mechanical Properties of Lipid Mono- and Bilayers. *Mol. Cryst. Liq. Cryst.* **449**, 95–106  
598 (2006).

This is the author's peer reviewed, accepted manuscript. However, the online version of record will be different from this version once it has been copyedited and typeset.

PLEASE CITE THIS ARTICLE AS DOI: 10.1063/5.0193333

- 598 34. Nagle, J. F., Jablin, M. S. & Tristram-Nagle, S. Sugar does not affect the bending and  
599 tilt moduli of simple lipid bilayers. *Chem. Phys. Lipids* **196**, 76–80 (2016).  
600 35. Dimova, R. Recent developments in the field of bending rigidity measurements on  
601 membranes. *Adv. Colloid Interface Sci.* **208**, 225–234 (2014).  
602 36. Gracià, R. S., Bezlyepkina, N., Knorr, R. L., Lipowsky, R. & Dimova, R. Effect of  
603 cholesterol on the rigidity of saturated and unsaturated membranes: fluctuation and  
604 electrodeformation analysis of giant vesicles. *Soft Matter* **6**, 1472 (2010).  
605 37. Eid, J., Razmazma, H., Jraij, A., Ebrahimi, A. & Monticelli, L. On Calculating the  
606 Bending Modulus of Lipid Bilayer Membranes from Buckling Simulations. *J. Phys. Chem.*  
607 *B* **124**, 6299–6311 (2020).  
608 38. Nagle, J. F. *et al.* A needless but interesting controversy. *Proc. Natl. Acad. Sci.* **118**,  
609 e2025011118 (2021).  
610 39. Pan, J., Tristram-Nagle, S. & Nagle, J. F. Effect of cholesterol on structural and  
611 mechanical properties of membranes depends on lipid chain saturation. *Phys. Rev. E* **80**,  
612 021931 (2009).  
613 40. Pöhl, M., Trollmann, M. F. W. & Böckmann, R. A. Nonuniversal impact of cholesterol  
614 on membranes mobility, curvature sensing and elasticity. *Nat. Commun.* **14**, 8038 (2023).  
615 41. Sturzenegger, F., Robinson, T., Hess, D. & Dittrich, P. S. Membranes under shear stress:  
616 visualization of non-equilibrium domain patterns and domain fusion in a microfluidic device.  
617 *Soft Matter* **12**, 5072–5076 (2016).  
618 42. Manning, M. L., Foty, R. A., Steinberg, M. S., Schoetz, E.-M. & Honig, B. H. Coaction  
619 of intercellular adhesion and cortical tension specifies tissue surface tension. *Proc. Natl.*  
620 *Acad. Sci. U. S. A.* **107**, 12517–12522 (2010).  
621 43. Aoki, T., Ohashi, T., Matsumoto, T. & Sato, M. The pipette aspiration applied to the  
622 local stiffness measurement of soft tissues. *Ann. Biomed. Eng.* **25**, 581–587 (1997).  
623 44. Dagan, Z., Weinbaum, S. & Pfeffer, R. An infinite-series solution for the creeping  
624 motion through an orifice of finite length. *J. Fluid Mech.* **115**, 505 (1982).  
625 45. Kosheleva, N. V. *et al.* Cell spheroid fusion: beyond liquid drops model. *Sci. Rep.* **10**,  
626 12614 (2020).  
627 46. Pajic-Lijakovic, I., Eftimie, R., Milivojevic, M. & Bordas, S. P. A. Multi-scale nature  
628 of the tissue surface tension: Theoretical consideration on tissue model systems. *Adv. Colloid*  
629 *Interface Sci.* **315**, 102902 (2023).  
630 47. Foty, R. A., Forgacs, G., Pflieger, C. M. & Steinberg, M. S. Liquid properties of  
631 embryonic tissues: Measurement of interfacial tensions. *Phys. Rev. Lett.* **72**, 2298–2301  
632 (1994).  
633 48. Forgacs, G., Foty, R. A., Shafir, Y. & Steinberg, M. S. Viscoelastic Properties of Living  
634 Embryonic Tissues: a Quantitative Study. *Biophys. J.* **74**, 2227–2234 (1998).  
635 49. Mary, G. *et al.* All-in-one rheometry and nonlinear rheology of multicellular aggregates.  
636 *Phys. Rev. E* **105**, 054407 (2022).  
637 50. Urbanska, M. *et al.* A comparison of microfluidic methods for high-throughput cell  
638 deformability measurements. *Nat. Methods* **17**, 587–593 (2020).  
639

#### 640 Acknowledgements

641 This work was supported in part by CNRS through the PICS CNRS program “Microfluidics for  
642 Soft Matter”, and by INSIS-CNRS. This work was partly supported by LAAS-CNRS micro  
643 and nanotechnologies platform member of the French RENATECH network. BGB was  
644 supported by a fellowship from the “Programa Propio de I+D+I 2022” of Universidad  
645 Politécnica de Madrid. Funding by “ADI, Université de Toulouse, Région Occitanie”, and by  
646 Federation Fermat, Université de Toulouse, are acknowledged. We thank Benjamin Reig for  
647 SEM imaging, Sandrine Souleille for microfluidics experiments, Charline Blatché for cell

This is the author's peer reviewed, accepted manuscript. However, the online version of record will be different from this version once it has been copyedited and typeset.

PLEASE CITE THIS ARTICLE AS DOI: 10.1063/1.5019333

648 culture, and Julien Roul for help in microscopy experiments. We thank Karine Guevorkian and  
649 Gregory Beaune for gently providing the S180 cell line.

650

651 **Author Contributions**

652 ME, HA, MP realized experiments on GUVs. SL, ME, PL realized experiments on spheroids.  
653 SL and BGB realized experiments on single cells. SL, ME, PL, HA, MP, AL, FM, DB  
654 contributed to chip fabrications. LM, JB calibrated the photolithography process. DB, CM, MD,  
655 CR, PJ contributed to experiments and supervised the research. PJ and SL wrote a first draft of  
656 the manuscript, all authors read and amended the manuscript.

657

658 **Competing interests**

659 There are no conflicts to declare.

660 Correspondence and requests for materials should be addressed to [pierre.joseph@laas.fr](mailto:pierre.joseph@laas.fr).